



Article

ZnWO₄ Nanoparticle Scintillators for High Resolution X-ray Imaging

Heon Yong Jeong, Hyung San Lim, Ju Hyuk Lee, Jun Heo, Hyun Nam Kim and Sung Oh Cho *

Department of Nuclear and Quantum Engineering, Korea Advanced Institute of Science and Technology (KAIST), Daejeon 34141, Korea; jeong93@kaist.ac.kr (H.Y.J.); samsterdam@kaist.ac.kr (H.S.L.); aragorn477@kaist.ac.kr (J.H.L.); heojun@kaist.ac.kr (J.H.); trexpp@kaist.ac.kr (H.N.K.)

* Correspondence: socho@kaist.ac.kr; Tel.: +82-(0)42-350-3823; Fax: +82-(0)42-350-3810

Received: 21 August 2020; Accepted: 29 August 2020; Published: 31 August 2020



Abstract: The effect of scintillator particle size on high-resolution X-ray imaging was studied using zinc tungstate (ZnWO₄) particles. The ZnWO₄ particles were fabricated through a solid-state reaction between zinc oxide and tungsten oxide at various temperatures, producing particles with average sizes of 176.4 nm, 626.7 nm, and 2.127 μm; the zinc oxide and tungsten oxide were created using anodization. The spatial resolutions of high-resolution X-ray images, obtained from utilizing the fabricated particles, were determined: particles with the average size of 176.4 nm produced the highest spatial resolution. The results demonstrate that high spatial resolution can be obtained from ZnWO₄ nanoparticle scintillators that minimize optical diffusion by having a particle size that is smaller than the emission wavelength.

Keywords: nanoparticle; scintillator; zinc tungstate; X-ray; spatial resolution

1. Introduction

Digital X-ray imaging utilizes a converter which produces visible light (indirect) or electrons (direct) after absorbing X-rays. An indirect setup uses a scintillator as a converter coupled with a light detector [1–4]. A scintillator is a substance that emits visible light when exposed to X-rays or other forms of radiation. Powder scintillators are used ubiquitously in various industries, especially in those involving medical diagnostics and non-destructive testing [5–9]. Currently, many efforts are being made to identify small components within objects utilizing non-destructive testing with X-rays [10–12]. The general approach to achieving this is to use micro-focus X-ray tubes [10], which are, unfortunately, expensive and bulky. Another way of managing this is to utilize a high-resolution X-ray imaging system comprising a scintillator and a detector with a pixel size as small as several hundred nanometers when coupled with an optical lens [11,12]. The system utilizes X-rays to generate images with the scintillator positioned directly under the object of interest. The X-ray images generated by the scintillator are magnified by the optical lens.

Producing high spatial resolution is one of the most defining characteristics of high-resolution X-ray imaging [13]. Spatial resolution is affected by the structure of a scintillator [14–16]; thus, powder scintillators are commonly used for high-resolution X-ray imaging [13] as they are easy to handle and manipulate [11,17]. However, currently available powder scintillators are composed of particles that are micrometers in size [18,19], leading to optical diffusion and, ultimately, reduction in spatial resolution when the scintillators are applied to produce X-ray images [20–22].

To address this issue, there have been past studies to increase the spatial resolution of X-ray images by implementing nanoparticle scintillators [18,23]; the relatively small particle size mitigates optical diffusion. Liaparinos, P.F. analyzed the effect of scintillator grain size ranging from 1 to 1000 nm using Monte Carlo simulation based on Mie scattering theory [18]. The results from this paper showed that

low optical diffusion can be achieved with nanoparticles. Cha, B.K., et al. produced europium-doped Gadolinium oxide ($Gd_2O_3:Eu$) nanoparticles and applied them to high-resolution X-ray imaging [23]. However, the effective pixel size of the detector used in the paper was far too large at 43 μm , and the study had issues with particle aggregation, leading to experimental failure.

In this study, zinc tungstate ($ZnWO_4$) particles of various sizes were used to determine the effect of particle size on high-resolution X-ray imaging. $ZnWO_4$ is a material of great interest in regard to being used as ultraviolet, X-ray, γ -ray, electron beam and proton beam scintillators [15–19], as the material is of low price and possesses excellent luminescence property, high density, high chemical stability, short decay time, and low afterglow [24–31]. The zinc oxide and tungsten oxide nanoparticles, used for fabricating $ZnWO_4$, were synthesized using anodization. Subsequently, $ZnWO_4$ nanoparticles were fabricated through a solid-state reaction between the as-prepared zinc oxide and tungsten oxide nanoparticles. The solid-state reaction was carried out at various temperatures to produce $ZnWO_4$ particles of varying sizes. A thin layer of the particles was applied onto silicon substrates to be used as scintillators in high-resolution X-ray imaging, and the effective pixel size of the detector used in this study is less than 1 μm .

2. Materials and Methods

2.1. Materials

Zinc and tungsten wires were purchased from Goodfellow (Huntingdon, UK). Potassium chloride (KCl) powder, ammonium fluoride (NH_4F) powder and polyethylene glycol (PEG, average molecular weight 200) were purchased from Sigma-Aldrich (St. Louis, MO, USA).

2.2. Fabrication and Characterization of $ZnWO_4$ Particles

Voltages of 15 V and 80 V were applied to deionized (DI) water electrolyte solutions containing 1 M KCl and 1 M NH_4F , respectively, to produce zinc oxide and tungsten oxide nanoparticles, respectively, via anodization. Anodization involves applying a voltage to a platinum electrode (–) and a metal wire (+) in an electrolyte solution, which leads to the oxidation and etching of the metal wire, resulting in the formation of metal oxide nanoparticles [32]. The nanoparticles were then extracted, washed with DI water, and dried in air at 60 °C. Afterwards, appropriate amounts of zinc oxide and tungsten oxide nanoparticles were added to DI water containing 0.2 wt% PEG to create solutions with a 1:1 atomic ratio between zinc and tungsten. The solutions were thoroughly mixed through sonication and vibrating ball milling, and then dried in air at 60 °C. The resulting powders were heated in an electric furnace at 700, 800, and 900 °C for 1 h to induce the solid-state reaction.

The structures of zinc oxide and tungsten oxide nanoparticles were analyzed using a field emission scanning electron microscope (FE-SEM, FEI MAGELLAN 400, FEI, Hillsboro, OR, USA). Further analyses were conducted using a transmission electron microscope (TEM, Titan cubed G2 60-300, FEI, Hillsboro, OR, USA) equipped with an energy dispersive X-ray spectroscopy (EDX) detector system (4 SDD Super X-detector system, FEI, Hillsboro, OR, USA). The structures of the fabricated $ZnWO_4$ particles were also analyzed with a FE-SEM. The crystallinity of the $ZnWO_4$ particles was analyzed using a high-resolution X-ray diffraction spectrometer (HR-XRD, SmartLab, Rigaku, Tokyo, Japan) with an analysis 2θ angle range of 10–90°.

2.3. Fabrication of $ZnWO_4$ Scintillator

The fabricated $ZnWO_4$ particles were mixed in DI water containing 0.2 wt% PEG and the mixture was ball-milled for 1 h to produce $ZnWO_4$ paste. Subsequently, the $ZnWO_4$ scintillators were developed by drop-casting the fabricated $ZnWO_4$ particles onto 150 μm silicon glass substrates (1.5 cm \times 1.5 cm) to a thickness of 10 μm .

3. Results and Discussion

3.1. Analyses of Nanoparticles Synthesized by Anodization

The zinc oxide and tungsten oxide nanoparticles were prepared by anodization. Figure 1a,b are the images of zinc oxide nanoparticles acquired using the FE-SEM and TEM, respectively. The images show that the nanoparticles are spherical with a size of 20–40 nm. The FE-SEM and TEM images of tungsten oxide nanoparticles are shown in Figure 1d,e respectively. The images show that tungsten oxide nanoparticles are in the shape of a plate with a width of 20–60 nm. Figure 1c,f show EDX spectra obtained from the zinc oxide and tungsten oxide nanoparticles, respectively. Both EDX spectra have an oxygen peak, confirming that the nanoparticles were indeed oxidized; the observed copper and carbon peaks are from the use of TEM grids (carbon film on 300-mesh copper).

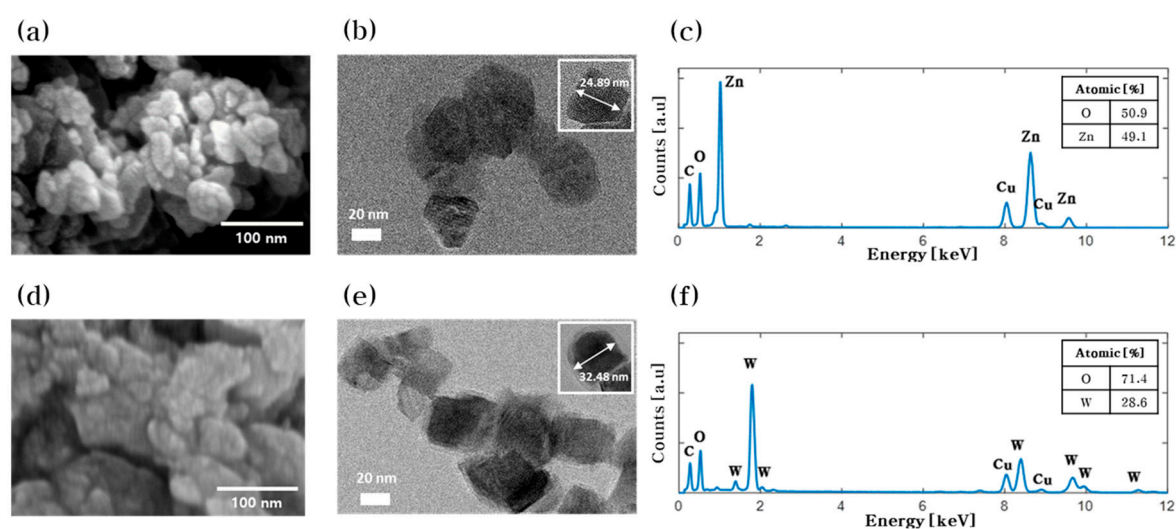


Figure 1. Metal oxide nanoparticles synthesized by anodization. (a) FE-SEM image, (b) TEM image, and (c) EDX spectrum of zinc oxide nanoparticles. (d) FE-SEM image, (e) TEM image, and (f) EDX spectrum of tungsten oxide nanoparticles.

3.2. Structure of $ZnWO_4$ Scintillator

The $ZnWO_4$ powders were fabricated by solid-state reaction at different temperature at 700, 800 and 900 °C. The structure morphology of $ZnWO_4$ powders are showed in Figure 2 by FE-SEM. The $ZnWO_4$ powders were sized through FE-SEM. As a result, the average sizes of powders fabricated at 700, 800 and 900 °C were 176.4 nm, 626.7 nm and 2.127 μ m respectively. This phenomenon of particle size increase resulting from reaction temperature elevation can be explained by oriented attachment growth during the solid-state reaction [33]. From a thermodynamics viewpoint, the driving force behind oriented attachment growth is reduction in free surface energy after particle mergence [34,35]. The $ZnWO_4$ powders fabricated at 700 and 800 °C were formed in the wavelength band of light or smaller, and the size of the powders fabricated at 900 °C were formed to micro-sized particles larger than the wavelength of light. Figure 3 shows the XRD patterns of the $ZnWO_4$ powders with an analysis 2θ range 10–90 °C. Comparing the peak value of the XRD pattern with the standard card (PDF ICDD card #01-078-0251), these powders crystallized into pure monoclinic $ZnWO_4$.

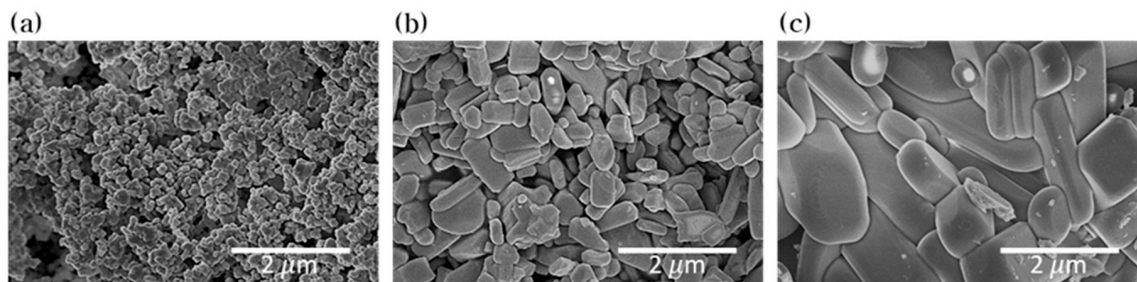


Figure 2. FE-SEM images of ZnWO₄ fabricated at (a) 700 °C, (b) 800 °C, and (c) 900 °C.

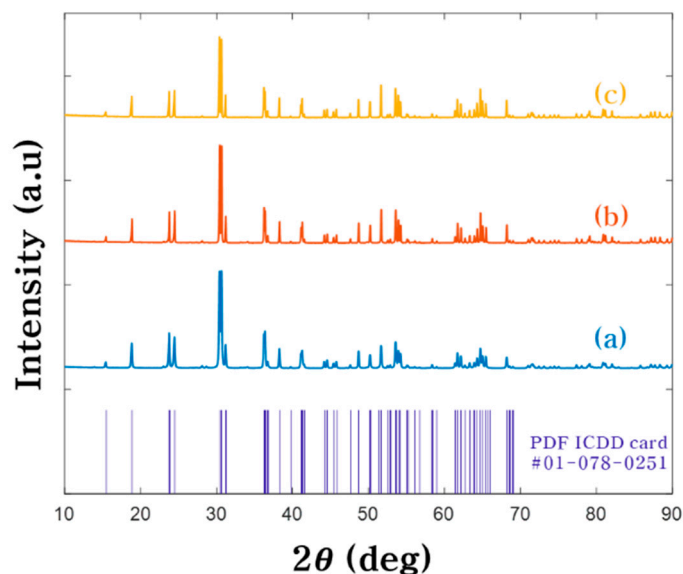


Figure 3. XRD spectra of ZnWO₄ fabricated at (a) 700 °C, (b) 800 °C, and (c) 900 °C.

3.3. Evaluation of X-ray Imaging Performance in High-resolution X-ray Imaging

The fabricated scintillator screens were implemented into a high-resolution X-ray imaging system (Figure 4). This system consists of a carbon nanotube (CNT) based miniature X-ray tube, a scintillator, an optical lens, and a scientific complementary metal-oxide-semiconductors (sCMOS) detector. The X-ray tube utilizes a CNT based electron beam emitter with an operating voltage and current of 50 kV_p and 0.35 mA, respectively. The focusing lens, attached to the X-ray tube, is cylindrical with an outer diameter of 40 mm and a height of 9 mm and is comprised of permanent magnets (NdFeB). The focal spot size of the miniature X-ray tube with the focusing lens is 337–390 μm [26]. A 10x optical lens is used to magnify the images produced by the scintillator and a sCMOS detector is used to develop the images. The pixel size of the sCMOS detector is 6.5 μm, but when coupled with the optical lens, the effective pixel size is reduced to 0.65 μm.

The relative emission intensities from the three fabricated ZnWO₄ scintillators, each with a different particle size, were measured using the high-resolution X-ray imaging system. The emission intensity values were determined by averaging the pixel values of X-ray images obtained at the same exposure condition. The results indicate no significant differences in emission level between the ZnWO₄ scintillators (Figure S1). The modulation transfer functions (MTFs) were measured to evaluate the spatial resolutions for the fabricated ZnWO₄ particles. This procedure is highly common in the field of X-ray imaging [12,23,36–38]. X-ray images of an edge of a 0.5 cm thick tungsten block were developed using the high-resolution X-ray imaging fitted with the fabricated ZnWO₄ scintillator screens. The edge spread functions (ESFs) were determined from the obtained X-ray images and, in turn, the MTFs were determined from the ESFs. The MTF curves obtained from utilizing the different scintillator screens are

shown in Figure 5a. The spatial frequency values of 278.2, 204.1, and 124.1 lp/mm were achieved from the average particle sizes of 176.4 nm, 626.7 nm, and 2.127 μm , respectively, at the MTF value of 10%.

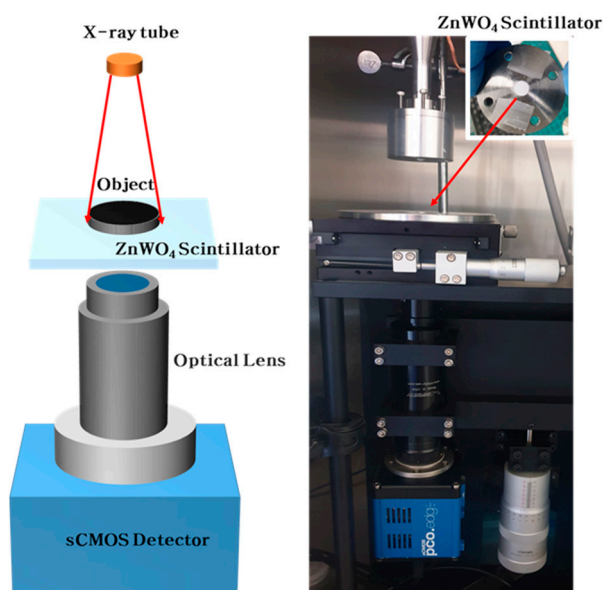


Figure 4. Applying ZnWO₄ scintillator screen to high-resolution X-ray imaging system.

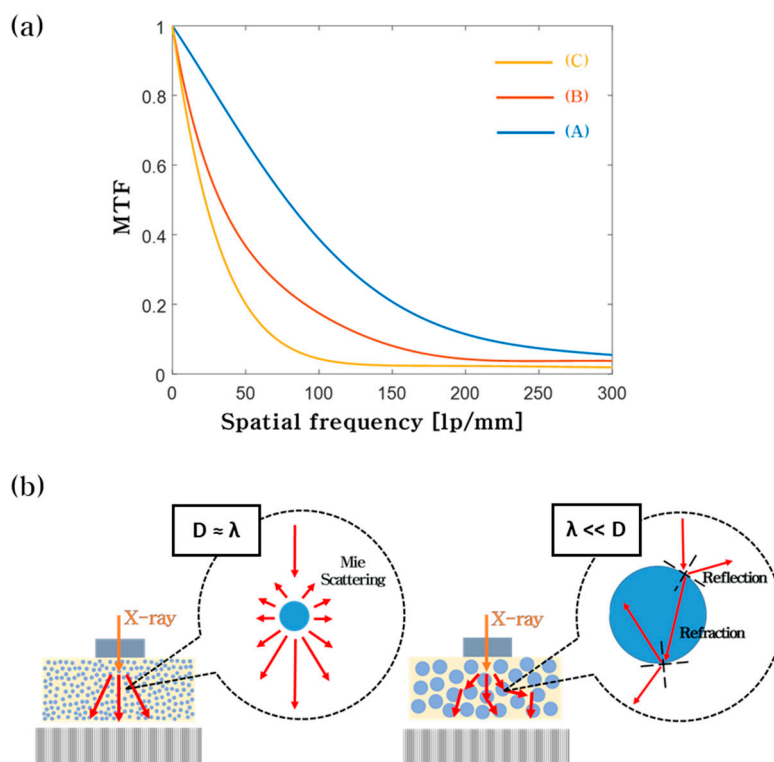


Figure 5. (a) MTF curves obtained from ZnWO₄ particles with sizes of (A) 176.4 nm, (B) 626.7 nm, and (C) 2.127 μm . (b) The effect of scintillator size on the spatial resolution of an X-ray image.

The reduction in spatial frequency resulting from particle size increase can be explained by the mechanism behind optical diffusion. For particles with a size much greater than the emission wavelength (λ), geometrical optics apply [39,40]. With such particles, light is reflected and refracted at the particle surface, causing significant light scatter. This is the case for the ZnWO₄ particles with an average size of 2.127 μm , resulting in the application of the particles producing the lowest frequency

among the frequency values obtained. When the particle size is comparable to the emission wavelength, Mie scattering becomes relevant [41,42]. Mie scattering is a phenomenon that causes the probability of light scatter to decrease steeply with decreasing particle size [43–45]. The ZnWO_4 emission spectrum covers a wavelength range of 400–600 nm when excited by X-rays at room temperature [24]. To verify, the photoluminescence (PL) spectra of the ZnWO_4 particles of different sizes were measured with a PL spectrometer (RAMBOSS-Star, DONGWOO OPTRON, Gyeonggi-do, Korea) equipped with a UV laser (325 nm He-Cd Laser, Kimmon, Tokyo, Japan). All spectra were close to identical and roughly covered a wavelength range of 400–600 nm (Figure S2). Thus, it can be expected that the 176.4 nm particles exhibit the highest spatial frequency.

Figure 6 shows the X-ray images of 300-mesh copper TEM grid obtained from the high-resolution X-ray imaging system. Consistent with the MTF results, a smaller particle size leads to a higher image resolution. The small effective pixel size (0.65 μm) allows for the inspection of small objects, however, causes the system to be sensitive to light scatter. Thus, it can be concluded that the use of small nanoparticles is optimal in improving the spatial resolution of X-ray images.

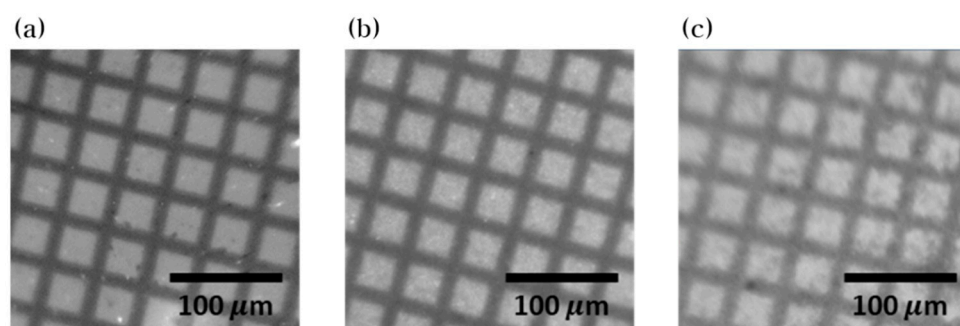


Figure 6. X-ray images of a TEM grid obtained from utilizing ZnWO_4 scintillator screens with average particles sizes of (a) 176.4 nm, (b) 626.7 nm, and (c) 2.127 μm .

4. Conclusions

The ZnWO_4 scintillator particles were fabricated through anodization and a solid-state reaction. The fabricated particles were then applied to high-resolution X-ray imaging to evaluate the spatial resolutions of the produced X-ray images. The experimental results showed that the optimal spatial resolution is achieved when the average particle size is less than the emission wavelength. The ZnWO_4 nanoparticles (100–250 nm), developed in our study, can be expected to reduce optical diffusion and provide spatial resolution. Furthermore, the significance of our results is not limited to ZnWO_4 particles; it can also be applied to other scintillator particles.

Supplementary Materials: The following are available online at <http://www.mdpi.com/2079-4991/10/9/1721/s1>, Figure S1: The emission intensities of ZnWO_4 scintillator screens with average particles sizes of (a) 176.4 nm (700 °C), (b) 626.7 nm (800 °C), and (c) 2.127 μm (900 °C); Figure S2: PL spectra of ZnWO_4 particles with average particles sizes of (a) 176.4 nm, (b) 626.7 nm, and (c) 2.127 μm .

Author Contributions: Conceptualization, and methodology, H.Y.J. and S.O.C.; formal analysis and investigation, H.Y.J., H.S.L., J.H.L., J.H. and H.N.K.; writing—original draft preparation, writing—review and editing, all authors. All authors have read and agreed to the published version of the manuscript.

Funding: This work was funded by the National Research Foundation of Korea (NRF) grant funded by the Korea government. (Grant number: NRF-2020M2D8A2069727).

Conflicts of Interest: The authors declare no conflict of interest.

References

1. Svenonius, O.; Sahlholm, A.; Wiklund, P.; Linnros, J. Performance of an X-ray imaging detector based on a structured scintillator. *Nucl. Instrum. Methods Phys. Res. Sect. A Accel. Spectrom. Detect. Assoc. Equip.* **2009**, *607*, 138–140. [[CrossRef](#)]
2. Smith, K.; Getzin, M.; Garfield, J.J.; Suvarnapathaki, S.; Camci-Unal, G.; Wang, G.; Gkikas, M. Nanophosphor-based contrast agents for spectral X-ray imaging. *Nanomaterials* **2019**, *9*, 1092. [[CrossRef](#)] [[PubMed](#)]
3. Chen, Q.; Wu, J.; Ou, X.; Huang, B.; Almutlaq, J.; Zhumekenov, A.A.; Guan, X.; Han, S.; Liang, L.; Yi, Z. All-inorganic perovskite nanocrystal scintillators. *Nature* **2018**, *561*, 88–93. [[CrossRef](#)] [[PubMed](#)]
4. Lempicki, A.; Brecher, C.; Szupryczynski, P.; Lingertat, H.; Nagarkar, V.V.; Tipnis, S.V.; Miller, S.R. A new lutetia-based ceramic scintillator for X-ray imaging. *Nucl. Instrum. Methods Phys. Res. Sect. A Accel. Spectrom. Detect. Assoc. Equip.* **2002**, *488*, 579–590. [[CrossRef](#)]
5. Michail, C.; Valais, I.; Seferis, I.; Kalyvas, N.; David, S.; Fountos, G.; Kandarakis, I. Measurement of the luminescence properties of Gd₂O₂S: Pr, Ce, F powder scintillators under X-ray radiation. *Radiat. Meas.* **2014**, *70*, 59–64. [[CrossRef](#)]
6. Rowlands, J. The physics of computed radiography. *Phys. Med. Biol.* **2002**, *47*, R123. [[CrossRef](#)]
7. Michail, C.; David, S.; Liaparinos, P.; Valais, I.; Nikolopoulos, D.; Kalivas, N.; Toutountzis, A.; Cavouras, D.; Kandarakis, I.; Panayiotakis, G. Evaluation of the imaging performance of LSO powder scintillator for use in X-ray mammography. *Nucl. Instrum. Methods Phys. Res. Sect. A Accel. Spectrom. Detect. Assoc. Equip.* **2007**, *580*, 558–561. [[CrossRef](#)]
8. Adam, J.; Metzger, W.; Koch, M.; Rogin, P.; Coenen, T.; Atchison, J.S.; König, P. Light emission intensities of luminescent Y₂O₃: Eu and Gd₂O₃: Eu particles of various sizes. *Nanomaterials* **2017**, *7*, 26. [[CrossRef](#)]
9. Nagarkar, V.V.; Millera, S.R.; Tipnis, S.V.; Lempicki, A.; Brecher, C.; Lingertat, H. A new large area scintillator screen for X-ray imaging. *Nucl. Instrum. Methods Phys. Res. Sect. B Beam Interact. Mater. At.* **2004**, *213*, 250–254. [[CrossRef](#)]
10. Tippkötter, R.; Eickhorst, T.; Taubner, H.; Gredner, B.; Rademaker, G. Detection of soil water in macropores of undisturbed soil using microfocus X-ray tube computerized tomography (μ CT). *Soil Tillage Res.* **2009**, *105*, 12–20. [[CrossRef](#)]
11. Martin, T.; Koch, A. Recent developments in X-ray imaging with micrometer spatial resolution. *J. Synchrotron Radiat.* **2006**, *13*, 180–194. [[CrossRef](#)] [[PubMed](#)]
12. Kim, H.N.; Jeong, H.Y.; Lee, J.H.; Cho, S.O. Development of a high resolution X-ray inspection system using a carbon nanotube based miniature X-ray tube. *Rev. Sci. Instrum.* **2020**, *91*, 043703. [[CrossRef](#)] [[PubMed](#)]
13. Touš, J.; Blažek, K.; Pína, L.; Sopko, B. High-resolution X-ray imaging CCD camera based on a thin scintillator screen. *Radiat. Meas.* **2007**, *42*, 925–928. [[CrossRef](#)]
14. Farman, T.T.; Vandre, R.H.; Pajak, J.C.; Miller, S.R.; Lempicki, A.; Farman, A.G. Effects of scintillator on the modulation transfer function (MTF) of a digital imaging system. *Oral Surg. Oral Med. Oral Pathol. Oral Radiol. Endodontol.* **2005**, *99*, 608–613. [[CrossRef](#)]
15. Trotta, C.; Massari, R.; Palermo, N.; Scopinaro, F.; Soluri, A. New high spatial resolution portable camera in medical imaging. *Nucl. Instrum. Methods Phys. Res. Sect. A: Accel. Spectrometers Detect. Assoc. Equip.* **2007**, *577*, 604–610. [[CrossRef](#)]
16. Nagarkar, V.V.; Gupta, T.K.; Miller, S.R.; Klugerman, Y.; Squillante, M.R.; Entine, G. Structured CsI (Tl) scintillators for X-ray imaging applications. *IEEE Trans. Nucl. Sci.* **1998**, *45*, 492–496. [[CrossRef](#)]
17. Fiserova, L.; Janda, J. Scintillation powders for the detection of neutrons. *IEEE Trans. Nucl. Sci.* **2018**, *65*, 2140–2146. [[CrossRef](#)]
18. Liaparinos, P.F. Optical diffusion performance of nanophosphor-based materials for use in medical imaging. *J. Biomed. Opt.* **2012**, *17*, 126013. [[CrossRef](#)]
19. Michail, C.; Kalyvas, N.; Valais, I.; Fudos, I.; Fountos, G.; Dimitropoulos, N.; Koulouras, G.; Kandris, D.; Samarakou, M.; Kandarakis, I. Image Quality Assessment of a CMOS/Gd₂O₂S: Pr, Ce, F X-ray Sensor. *J. Sens.* **2015**, *2015*, 874637:1–874637:6. [[CrossRef](#)]
20. Poludniowski, G.G.; Evans, P.M. Optical photon transport in powdered-phosphor scintillators. Part 1. Multiple-scattering and validity of the Boltzmann transport equation. *Med. Phys.* **2013**, *40*, 041904. [[CrossRef](#)]

21. Chen, G.; Johnson, J.; Weber, R.; Nishikawa, R.; Schweizer, S.; Newman, P.; MacFarlane, D. Fluorozirconate-based nanophase glass ceramics for high-resolution medical X-ray imaging. *J. Non-Cryst. Solids* **2006**, *352*, 610–614. [[CrossRef](#)]
22. Ohashi, Y.; Yasui, N.; Yokota, Y.; Yoshikawa, A.; Den, T. Submicron-diameter phase-separated scintillator fibers for high-resolution X-ray imaging. *Appl. Phys. Lett.* **2013**, *102*, 051907. [[CrossRef](#)]
23. Cha, B.K.; Lee, S.J.; Muralidharan, P.; Kim, J.Y.; Kim, D.K.; Cho, G. Characterization and imaging performance of nanoscintillator screen for high resolution X-ray imaging detectors. *Nucl. Instrum. Methods Phys. Res. Sect. A Accel. Spectrometers Detect. Assoc. Equip.* **2011**, *633*, S294–S296.
24. Kraus, H.; Mikhailik, V.; Ramachers, Y.; Day, D.; Hutton, K.; Telfer, J. Feasibility study of a ZnWO₄ scintillator for exploiting materials signature in cryogenic WIMP dark matter searches. *Phys. Lett. B* **2005**, *610*, 37–44. [[CrossRef](#)]
25. Fu, H.; Lin, J.; Zhang, L.; Zhu, Y. Photocatalytic activities of a novel ZnWO₄ catalyst prepared by a hydrothermal process. *Appl. Catal. A Gen.* **2006**, *306*, 58–67. [[CrossRef](#)]
26. Lou, Z.; Hao, J.; Cocivera, M. Luminescence of ZnWO₄ and CdWO₄ thin films prepared by spray pyrolysis. *J. Lumin.* **2002**, *99*, 349–354. [[CrossRef](#)]
27. Wang, K.; Feng, W.; Feng, X.; Li, Y.; Mi, P.; Shi, S. Synthesis and photoluminescence of novel red-emitting ZnWO₄: Pr³⁺, Li⁺ phosphors. *Spectrochim. Acta Part. A Mol. Biomol. Spectrosc.* **2016**, *154*, 72–75. [[CrossRef](#)]
28. Ryu, J.H.; Lim, C.S.; Auh, K.H. Synthesis of ZnWO₄ nanocrystalline powders, by the polymerized complex method. *Mater. Lett.* **2003**, *57*, 1550–1554. [[CrossRef](#)]
29. Wen, F.-S.; Zhao, X.; Huo, H.; Chen, J.-S.; Shu-Lin, E.; Zhang, J.-H. Hydrothermal synthesis and photoluminescent properties of ZnWO₄ and Eu³⁺-doped ZnWO₄. *Mater. Lett.* **2002**, *55*, 152–157. [[CrossRef](#)]
30. Dkhilalli, F.; Borchani, S.M.; Rasheed, M.; Barille, R.; Guidara, K.; Megdiche, M. Structural, dielectric, and optical properties of the zinc tungstate ZnWO₄ compound. *J. Mater. Sci. Mater. Electron.* **2018**, *29*, 6297–6307. [[CrossRef](#)]
31. Holl, I.; Lorenz, E.; Mageras, G. A measurement of the light yield of common inorganic scintillators. *IEEE Trans. Nucl. Sci.* **1988**, *35*, 105–109. [[CrossRef](#)]
32. Ali, G.; Park, Y.J.; Kim, J.W.; Cho, S.O. A Green, General, and Ultrafast Route for the Synthesis of Diverse Metal Oxide Nanoparticles with Controllable Sizes and Enhanced Catalytic Activity. *ACS Appl. Nano Mater.* **2018**, *1*, 6112–6122. [[CrossRef](#)]
33. Yang, Y.; Scholz, R.; Fan, H.J.; Hesse, D.; Gosele, U.; Zacharias, M. Multitwinned spinel nanowires by assembly of nanobricks via oriented attachment: A case study of Zn₂TiO₄. *ACS Nano* **2009**, *3*, 555–562. [[CrossRef](#)] [[PubMed](#)]
34. Niederberger, M.; Cölfen, H. Oriented attachment and mesocrystals: Non-classical crystallization mechanisms based on nanoparticle assembly. *Phys. Chem. Chem. Phys.* **2006**, *8*, 3271–3287. [[CrossRef](#)]
35. Zhang, Q.; Liu, S.J.; Yu, S.H. Recent advances in oriented attachment growth and synthesis of functional materials: Concept, evidence, mechanism, and future. *J. Mater. Chem.* **2009**, *19*, 191–207. [[CrossRef](#)]
36. Rossmann, K. Measurement of the modulation transfer function of radiographic systems containing fluorescent screens. *Phys. Med. Biol.* **1964**, *9*, 551. [[CrossRef](#)]
37. Gambaccini, M.; Taibi, A.; Del Guerra, A.; Marziani, M.; Tuffanelli, A. MTF evaluation of a phosphor-coated CCD for X-ray imaging. *Phys. Med. Biol.* **1996**, *41*, 2799. [[CrossRef](#)]
38. Kalivas, N.; Valais, I.; Salemis, G.; Karagiannis, C.; Konstantinidis, A.; Nikolopoulos, D.; Loudos, G.; Sakelios, N.; Karakatsanis, N.; Nikita, K. Imaging properties of cerium doped Yttrium Aluminum Oxide (YAP: Ce) powder scintillating screens under X-ray excitation. *Nucl. Instrum. Methods Phys. Res. Sect. A Accel. Spectrom. Detect. Assoc. Equip.* **2006**, *569*, 210–214. [[CrossRef](#)]
39. Yang, P.; Liou, K. An “exact” geometric-optics approach for computing the optical properties of large absorbing particles. *J. Quant. Spectrosc. Radiat. Transf.* **2009**, *110*, 1162–1177. [[CrossRef](#)]
40. Nousiainen, T.; Muinonen, K.; Räisänen, P. Scattering of light by large Saharan dust particles in a modified ray optics approximation. *J. Geophys. Res. Atmos.* **2003**, *108*, AAC 12-11–AAC 12-17. [[CrossRef](#)]
41. Ye, Q.-L.; Yoshikawa, H.; Bandow, S.; Awaga, K. Green magnetite (Fe₃O₄): Unusual optical Mie scattering and magnetic isotropy of submicron-size hollow spheres. *Appl. Phys. Lett.* **2009**, *94*, 063114. [[CrossRef](#)]
42. Bohren, C.F.; Huffman, D.R. *Absorption and Scattering of Light by Small Particles*; John Wiley & Sons: Hoboken, NJ, USA, 2008.

43. Moosmüller, H.; Sorensen, C. Small and large particle limits of single scattering albedo for homogeneous, spherical particles. *J. Quant. Spectrosc. Radiat. Transf.* **2018**, *204*, 250–255. [[CrossRef](#)]
44. Melling, A. Tracer particles and seeding for particle image velocimetry. *Meas. Sci. Technol.* **1997**, *8*, 1406. [[CrossRef](#)]
45. Chien, M.-H.; Brameshuber, M.; Rossboth, B.K.; Schütz, G.J.; Schmid, S. Single-molecule optical absorption imaging by nanomechanical photothermal sensing. *Proc. Nat. Acad. Sci. USA* **2018**, *115*, 11150–11155. [[CrossRef](#)] [[PubMed](#)]



© 2020 by the authors. Licensee MDPI, Basel, Switzerland. This article is an open access article distributed under the terms and conditions of the Creative Commons Attribution (CC BY) license (<http://creativecommons.org/licenses/by/4.0/>).